

Received March 25, 2019, accepted April 23, 2019, date of publication May 10, 2019, date of current version May 22, 2019.

Digital Object Identifier 10.1109/ACCESS.2019.2916153

Mechanical Properties of Rock With Intersection Structures and Its Progressive Failure Mechanism

SHAOWEI MA^{1,2}, ZHOUQUAN LUO^{1,2}, HAO WU^{1,2,3}, AND YAGUANG QIN^{1,2}

¹School of Resources and Safety Engineering, Central South University, Changsha 410083, China

²Hunan Key Laboratory of Mineral Resources Exploitation and Hazard Control for Deep Metal Mines, Changsha 410083, China

³Department of Mining and Geological Engineering, The University of Arizona, Tucson, AZ 85721, USA

Corresponding authors: Hao Wu (hoekwu@csu.edu.cn) and Yaguang Qin (csuqyg@163.com)

This work was supported in part by the National Key Research and Development Program of China during the Thirteenth Five Year Plan Period: The Continuous Mining Theory and Technology on Spatiotemporal Synergism of Multi-mining Areas within a Large Ore Block for Deep Metal Deposit under Grant 2017YFC0602901, and in part by the Fundamental Research Funds for the Central Universities of Central South University under 2018zzts215.

ABSTRACT To investigate the influence of intersection structures on the mechanical properties and failure mechanisms of rock materials, a series of uniaxial compression tests on complete red sandstone specimens and specimens with various hole shapes (T-shape, cross-shape, and shaft-roadway-shape) were conducted by the Instron 1346 servo-controlled rock mechanics testing machine. Flac3D software and digital image correlation (DIC) were used to simulate the internal stress distribution of rock specimens and reproduce the process of fracture, i.e., cracks initiate, propagate, and coalesce with each other into macroscopic failure under progressive loading. The results show that the intersection structure has a significant weakening effect on the mechanical properties of the rock. The rock strength, elastic modulus, and peak strain of specimens can be ranked as complete specimens > cross-shaped intersection structure specimens > T-shaped intersection structure specimens > shaft-roadway-shaped intersection structure specimens. The energy consumption ratio of the intersection structure specimens before the peak reaches more than 30%, which is approximately twice that of the intact specimens. The brittleness coefficients of the four types of specimens are 0.18, 0.26, 0.21, and 0.20, respectively. The intersection structure specimens induced different degrees of tensile and compressive stress concentration zones on the top and bottom sides of the intersection center point. As a result, initial tensile cracks parallel to the loading direction and shear cracks leading to spalling failure on both sides of the holes were formed. With the increase of the axial stress, secondary tensile cracks extending on the opposite direction appeared at the upper and lower corners of the hole. When the far-field cracks that propagated along the diagonal line coalesced with secondary tensile cracks, macro shear-failure of the specimens appeared. With the increase in axial stress, the principal strain monitored during the fracture process of the specimens gradually increased, then it slowly decreased after the peak. The arched boundary of the T-shaped intersection structure specimen had good stability because of its advantage of suppressing the occurrence of the spalling failure. The shaft-roadway-shaped intersection structure could provide compensation space for the secondary tensile cracks due to the existence of the vertical well. The degree of inhibition of initial tensile cracks was so small that the type of specimens was highly prone to instability or failure.

INDEX TERMS Intersection structures, digital image correlation (DIC), mechanical properties, failure mechanism, crack, brittleness, energy dissipation.

I. INTRODUCTION

To meet the needs of mining, underground mines often need to be excavated for a large number of roadway projects,

The associate editor coordinating the review of this manuscript and approving it for publication was Bora Onat.

such as shafts, roadways, and chambers. Considering the different functional requirements, mining technologies, and other factors, roadways often need to be crossed or branched, which forms a large number of intersection structures, such as the intersection point formed by the roadways, the ingate formed by the roadway and the shaft, and the funnel formed

by roadways, and raises such as ore chutes, pedestrian raises, ventilation, and filling raises. Because there is a large exposed area, a high stress concentration of surrounding rock and multiple excavation disturbances at the intersection, the effects of excavation disturbance and intersection structures easily lead to roof fall and rib spalling, which often need to be reinforced and seriously affect normal production. It is particularly necessary to study the stability and failure mechanisms of intersection structures in the design of shaft and drift support.

Scholars have conducted much research studies on surrounding rock stability and support technology for different types of intersection structures. With respect to roadway intersections, the U.S. Bureau of Mining (USBM) found that more than 30% of roof accidents for the room and pillar mining method occur at roadway intersections and that the surrounding rock stability at four-way intersections is the worst, with a maximum roof settlement twice as much as that at three-way intersections [1]. OKULO and PENGG [2] obtained by simulation that the roof of a three-way roadway intersection of roadway can easily form an arch-shaped tension stress area and the vertical tension stress in the area increases with the decrease of the intersection angle. Gercek [3], [4] considered that the higher the horizontal stress and the more complex the intersection structure of the roadway, the worse the stability of the roof at the intersection point and the wider the stress superposition area; a dome forms after the roof falls, and the support design of the intersection needs to be intensified and strengthened. Hematain [5] gave formulas for calculating the dome radius, the height of the four-way intersection point, the settlement of the roof and the floor heave at the intersection center point. The results showed that the dome bottom radius was $\sim 4.0\text{--}6.5$ m and the falling height was $\sim 1.5\text{--}7.5$ m. SINGHRN *et al.* [6] pointed out that there are four failure modes at a T-shaped intersection: dome-shaped shear failure, delamination tension fracture, buckling and compression grooving, and shear slip of geologically-weak surfaces. In addition, a 0.4-times vertical stress isoline of the roof is proposed as the dome fall boundary. Esterhuizen *et al.* [7] found that low horizontal stress and high horizontal stress are the main causes of delamination fracture and buckling grooving at an intersection. Abbasi [8] also explored the influence of the lateral pressure coefficient on the stability of surrounding rock at a four-way intersection. The results showed that the failure height of the roof increases and that the failure form changes from tensile failure to shear failure with the increase of the lateral pressure coefficient. Lu *et al.* [9] used FLAC3D software to analyze the influence of intersection form, depth, surrounding rock strength, excavation sequence and excavation step on the mechanical response of surrounding rock at an intersection. Huabin *et al.* [10] used ANSYS numerical analysis and orthogonal experiments to determine that rock mass strength is the main factor that affects the stability of intersection structures. Guo *et al.* [11] considered that the failure of Y-shaped intersections was caused by the lateral outburst of intermediate rock pillar fracturing.

Rihong *et al.* [12] simulated and analyzed the intersection-angle effect on the surrounding rock deformation at the intersection of a roadway and found that the deformation of surrounding rock increases with the decrease of the intersection-angle and migrates towards the sharp-angle side. In addition, Weisheng *et al.* [13] also discussed the effect of principal stress on the stability of an intersection. Aiming at the support design of surrounding rock after repairs at roadway intersections, Naibin *et al.* [14] designed the roof reinforcement scheme of chemical grouting and anchor cable reinforcement. Cheng *et al.* [15] developed the comprehensive control technology of pregrouting reinforcement, three-dimensional roof anchor cables, and prestressed trusses. Xiaoyi *et al.* [16] also developed the double-control anchor support technology based on the support idea of “strong and hard support”. A good control effect has been achieved by the above supporting methods.

Regarding the research aspect of stereoscopic intersection structures of mines, Manchao *et al.* [17] analyzed the variation regularity of stress and displacement of surrounding rock in the intersection structures of drainage chamber groups under different construction sequences and found that the excavation sequence of “first branch roadway and then main roadway” had the least disturbance to the intersection-structure. GUO *et al.* [18] considered that the deformation and instability of the intersection structures of deep chamber groups are the interactive results of high ground stress, unreasonable intensive layout, and unsuitable supporting technology. Xiang [19] studied the variation regularity of the stress and displacement of surrounding rock in an ingate excavation under the condition of a prefabricated wellbore by using a similar simulation experiment and found that the stress of surrounding rock above the ingate had a trend of first stability and then rapid release. In addition, the displacement of the surrounding rock above the ingate had a trend of first a slow and then a sharp increase, which was consistent with the convergence deformation law measured in the ingate of an auxiliary well in Zhuji mine. Hua *et al.* [20] revealed the distribution regularity of stress fields and plastic zones of a deep shaft connecting chamber groups by finite element numerical simulation and then developed and applied the combined support technology of bolt net shotcrete initial support and cast-in-place reinforced concrete secondary support. It can be seen from the above review that the current focus is on repair technology after the failure of intersection structure supports. Few studies have been made on evolution process of fractures and progressive failure mechanisms. However, the instability deformation of intersection structures is the process of crack initiation, propagation, and penetration under mining stress. When the mine enters the deep complex mining environment, the mechanical constitutive behavior of a rock mass is different from that of a shallow rock mass, which makes the roadway intersection structure failure mode more complex. In view of this, the authors conducted uniaxial compression tests on slab red sandstone with different types of prefabricated intersection structures, and observed the changes of

strain fields on the surface of the rock samples by means of the DIC measurement system to reveal the fracture evolution mechanism of surrounding rock with intersection structures and provide the basis for the design of intersection structure support.

II. DIC DIGITAL IMAGE DEFORMATION MEASUREMENT PRINCIPLE

Accurate acquisition of full-field real-time deformation is the precondition for mastering the fracture mechanics behavior of rock materials under different loads. Due to the uncertainty of the crack propagation path of rock, it is obvious that the traditional contact strain electrical measurement method cannot meet the requirements of the surface strain and displacement monitoring function. Digital image correlation technology proposed in the 1980s is an optical measurement method based on the computer vision principle, digital image processing, and numerical calculation [21-22]. It has been widely applied in the material field due to its advantages of a simple experimental equipment and measurement process, strong anti-interference ability, wide application range and high efficiency in identifying strain localization characteristics. In recent years, a few reports have been reported in the field of rock fracture mechanics.

The digital image correlation method obtains the displacement vector of the same pixel by tracking its position in two speckle images before and after surface deformation. Therefore, a random speckle field should be made on the surface of a rock observation area as the carrier of location information. In this paper, artificial speckles were made by randomly spraying black and white paint on the surface of the samples. The digital speckle image before deformation of rock monitoring area is called the reference image, and the deformed digital speckle image is called the deformed image. In the reference image, a square region with a size of $(2k + 1) \times (2k + 1)$ pixels is selected as the benchmark subset. The reason that a rectangular subset is chosen to be tracked instead of a single pixel is that the rectangular subset has a wider gray value range than a single pixel point, which is easier to identify [23]. In the deformed image, a large range region-covering subsets is selected as the search subset. In the search subset, a subset of the same size as that of the reference subset is selected as the deformed subset based on each pixel being the center. Then, a correlation function is used to make matching calculations of tracking and relevance for each deformed subset in reference subset and the search subset. The position corresponding to the extreme point of the correlation coefficient R is the deformed position of the reference subset, that is, the target subset. The central point of the target subset is the tracking point $P'(x_0', y_0')$ after the deformation of the measurement point, as shown in Fig. 1.

III. SAMPLE PREPARATION AND EXPERIMENTAL DESIGN
A. SELECTION OF INTERSECTION STRUCTURE TYPES

Based on the actual intersection structures of mines, three types of intersection structures were selected as the research

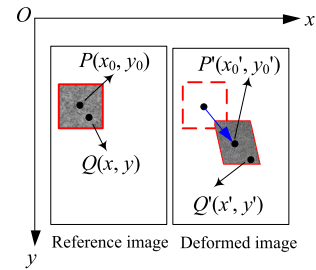


FIGURE 1. Schematic illustration of a subset before and after deformation.

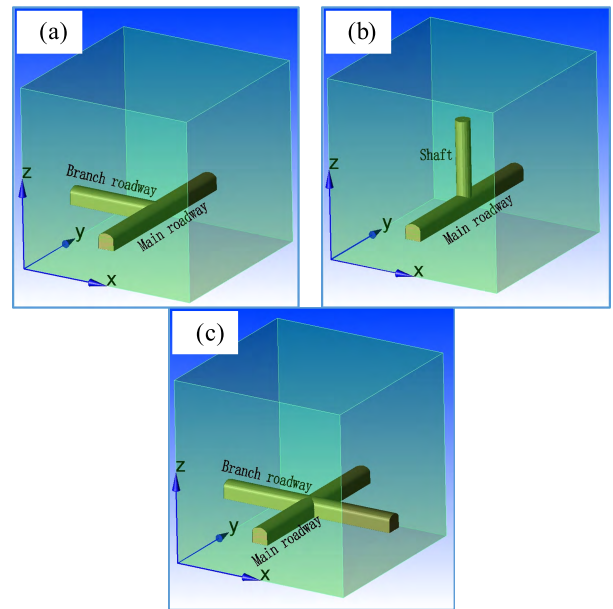


FIGURE 2. Schematic diagrams of three intersection structure types. (a) T-shaped intersection structure; (b) Cross-shaped intersection structure; (c) Shaft-roadway-shaped intersection structure.

objects, including T-shaped intersection structure, cross-shaped intersection structure and shaft-roadway-shaped intersection structure, as shown in Fig. 2. The section of main roadways and branch roadways is straight-wall semicircular arches, the ratio of roadway width to wall height is 4:1, and the section of the shaft is circular.

B. PREFABRICATION OF INTERSECTION STRUCTURE SPECIMENS

Because the three-dimensional crack propagation of rock is not easy to observe, the three-dimensional intersection problem is simplified as a plane stress problem. The mechanical response and crack propagation regularity of prefabricated intersection structure specimens under uniaxial compression were studied by making plate rock samples on the basis of intersection point center transverse profiles.

The samples were Shandong red sandstone and they had high integrity and homogeneity. Their main mineral components were feldspar and quartz, and their particle sizes were relatively uniform. Considering that the specimen should not be too thin and prone to buckling and instability failure, too

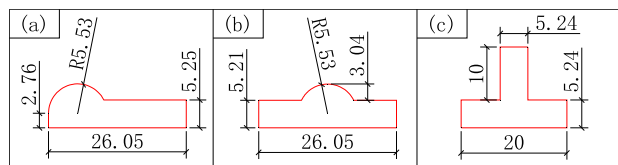


FIGURE 3. The size of the prefabricated intersection structures. (a) T-shaped intersection structure. (b) Cross-shaped intersection structure. (c) Shaft-roadway-shaped intersection structure.

thick and prone to three-dimensional cracks, that the ratio of height to diameter should not be too small and that the friction effect has a greater impact at the end of the specimen, the size of the specimen was set at 100 mm × 150 mm × 25 mm (length × height × thickness). In addition, the size of the prefabricated intersection structures is shown in Fig. 3, with units of mm.

In accordance with the recommendations and specifications of the International Committee on Rock Mechanics, a professional cutting mill was used to process the specimens to meet the requirement that the nonparallelism and nonperpendicularity of the four ends of the specimens should be less than 0.02 mm. Then, a total of 12 specimens were made, including 3 complete specimens used for comparison; the remaining 9 specimens were prefabricated as three types of intersection structures formed by hydraulic cutting with a SAME50HC three-axis cantilever water cutter with better forming quality, as shown in Fig. 4. To facilitate the analysis of the mechanical properties of samples with different types of intersection structures, their void areas were approximately equal. In addition, a series of standard specimens were taken to carry out the uniaxial compression test, Brazilian splitting test, and variable angle shear test. The physical and mechanical parameters of red sandstone measured in the laboratory were as follows: P -wave velocity was 3174 m/s, the density was 2.47 g/cm³, uniaxial compressive strength was 99.32 MPa, tensile strength was 5.28 MPa, elastic modulus was 24.35 GPa, Poisson's ratio was 0.26, internal friction angle was 40.43° and cohesion was 19.01 MPa.

C. TEST EQUIPMENT AND INSTRUMENTS

An Instron 1346 hydraulic servo rock mechanics experiment system was used to conduct the uniaxial compression test on the specimens. Its maximum range is 2000 kN and its load measurement accuracy is $\pm 0.5\%$. It can test the mechanical properties of rocks such as uniaxial tension, compression, shear, and bending. The axial displacement can be measured by an LVDT extensometer. In addition, the system can automatically collect the time travel curves of load and displacement. The DIC strain measurement system was used to measure the strain field of the specimen. Before the beginning of the experiment, the dust and other dirt on the surface of a sample were erased, and a thin layer of white SANVO brand bottled paint was sprayed on the surface of the plate specimen to form a smooth base. After drying, the black spray paint was sprayed on the white base to produce random speckles, which could not be so dark or so bright that the image quality

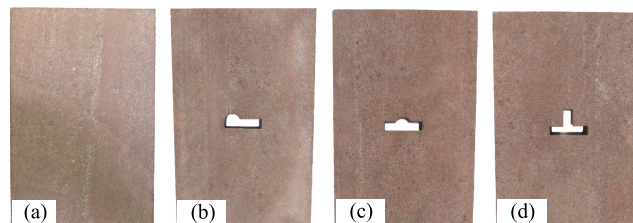


FIGURE 4. Different types of rock specimens prepared. (a) Complete specimen. (b) T-shaped intersection structure specimen. (c) Cross-shaped intersection structure specimen. (d) Shaft-roadway-shaped intersection structure specimen.



FIGURE 5. Uniaxial compression test system for specimens.

can't be guaranteed. The DIC strain measurement system was installed after the samples were coated with Vaseline on the upper and lower loading ends and placed on the press. A CCD industrial camera was required to align the center of the sample with a deviation angle of not more than 5° and with the lens approximately 1 m away from the sample. At the same time, a supplementary light lamp was installed on both sides of the sample to adjust the focal length and exposure time of the camera to ensure the best quality of the speckle image collected by the data acquisition system. The CCD industrial camera was a Basler PiA2400-17gm with a resolution of 2456 × 2568 pixels, a frame rate of 17 f/s and an image acquisition speed of 15 sheets/s. Data acquisition was centrally controlled by Pylon Viewer software installed in a computer, and the images were processed and analyzed by GOM Correlate software. The experimental system is shown in Fig. 5.

D. TEST DESIGN

At the beginning of the experiment, the rock mechanics testing machine and the DIC strain measuring system were simultaneously opened. The experiment was initially controlled by the force mode with a loading speed of 200 N/s, which was changed by the displacement-controlled loading mode with a displacement loading speed of 0.1 mm/min when the sample strength was approximately one-half (125 kN). It was found that the stress-strain curves of the specimens

TABLE 1. Basic parameters of specimens.

Specimen Type	Specimen Number	Length /mm	Thickness /mm	Height /mm	Density /kg·m ⁻³	Void Area /mm ²
Complete specimens	A-1	100.10	25.00	150.10	2391.37	0.00
	A-2	99.60	24.90	150.50	2427.49	
	A-3	100.70	24.80	150.70	2467.45	
T-shaped intersection structure specimens	B-1	100.50	23.00	150.80	2382.43	156.58
	B-2	100.20	24.80	151.00	2408.37	
	B-3	100.40	24.70	150.90	2439.81	
Cross-shaped intersection structure specimens	C-1	100.30	25.00	151.00	2461.65	157.08
	C-2	100.40	23.50	150.60	2439.30	
	C-3	100.50	25.00	150.50	2430.60	
Shaft-roadway-shaped intersection structure specimens	D-1	100.20	25.00	150.70	2424.91	157.20
	D-2	100.30	25.80	150.80	2433.99	
	D-3	100.60	23.40	150.50	2411.55	

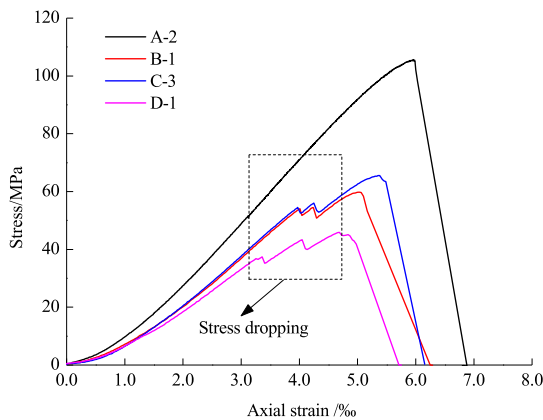


FIGURE 6. Stress-strain curves of specimens.

under this traditional laboratory loading mode exhibited large step oscillations during the elastic phase transition, which affected the magnitude of elastic modulus and peak strain. In addition, the strength of the intersection structure specimens was not easy to determine, which led to the switch time being difficult to determine. Considering the loading time and hard disk storage space, a 0.1 mm/min displacement loading mode could not meet the requirement of a large amount of image storage. Therefore, the displacement loading speed of the rock mechanics testing machine was set at 0.6 mm/min from the third specimen (A-3). Uniaxial compression tests were first conducted on three complete specimens and then on the other nine precast cross-structured rocks. The basic parameters of each specimen are shown in Tab. 1. The stress-strain curves of four types of rock samples are shown in Fig. 6.

IV. MECHANICAL PROPERTIES OF DIFFERENT SPECIMEN TYPE

A. CHANGE REGULATION OF SPECIMEN STRENGTH

The relevant mechanical parameters calculated from the stress-strain curves of the specimens are shown in Tab.2. It can be seen that the intersection structure has a significant weakening effect on rock strength and that the maximum weakening degree is more than 50%. The average peak

strengths of the complete specimen, T-shaped intersection structure specimen, cross-shaped intersection structure specimen, and shaft-roadway-shaped intersection structure specimen are 102.61 MPa, 61.64 MPa, 64.31 MPa, and 46.01 MPa, respectively. Among them, the bearing capacity of intersection structure rock samples is the worst, whereas the strength of the cross-shaped intersection structure specimen is slightly higher than that of the T-shaped intersection structure specimen, which shows that the less smooth the boundary of the intersection structure, the higher the stress concentration, and the more easily the specimen will be unstable. It can also be seen from Fig. 6 that the stress-strain curve of intersection structure specimens fluctuated before the peak, which was caused by the stress drop from the initiation and propagation of cracks in the rock specimens. In addition, all the specimen types showed nearly zero residual strength after the peak, which indicates that the rocks were remarkably brittle. The relevance of this feature to engineering is that the failure of deep high-stress hard rock is instantaneous and violent so that it needs timely support or advanced reinforcement after excavation. Unlike shallow plastic rock failure, deep hard rock does not have high residual strength and cannot be self-bearing or have allowable lag support.

B. DEFORMATION CHARACTERISTIC OF SPECIMENS

From the stress-strain curves in Fig. 6, it can be seen that all specimen types featured a remarkable brittleness. The postpeak deformation was small, and the prepeak deformation presented a typical S-shaped curve overall. The entire process of deformation consists of four stages: the fracture compaction closure stage, the elastic deformation stage, the plastic deformation stage, and the postpeak stage. The elastic modulus and peak strain of different types of specimens are shown in Fig. 7. It can be seen that the elastic modulus and peak strain of the specimens were basically consistent with the law of strength change, i.e., complete specimen > cross-shaped intersection structure specimen > T-shaped intersection structure specimen > shaft-roadway-shaped intersection structure specimen. The results show that the stiffness and brittleness of the complete specimen were

TABLE 2. Test results of specimens under axial loading.

Specimen Types	Specimen Number	Strength /MPa	Peak Strain /%	Elastic Modulus /GPa	Energy Absorption Density/kJ·m ⁻³	Energy Dissipation Density /kJ·m ⁻³	Brittleness Coefficient
Complete specimens	A-1	100.92	5.57	21.63	268.01	32.58	0.21
	A-2	105.61	5.96	21.63	298.52	40.70	0.16
	A-3	101.31	6.97	20.05	307.61	51.66	/
T-shaped intersection structure specimens	B-1	59.82	5.01	17.82	147.61	47.21	0.25
	B-2	58.47	5.10	17.48	155.52	57.73	0.06
	B-3	66.64	4.03	18.48	164.08	43.93	0.48
Cross-shaped intersection structure specimens	C-1	62.10	5.34	18.49	164.54	60.26	0.22
	C-2	65.30	4.77	19.01	159.48	47.33	0.25
	C-3	65.54	5.35	18.09	170.025	51.30	0.18
Shaft-roadway-shaped intersection structure specimens	D-1	45.92	4.69	14.91	106.68	35.97	0.27
	D-2	45.85	3.29	15.64	99.36	32.15	0.14
	D-3	46.25	5.22	14.46	117.10	43.14	0.17

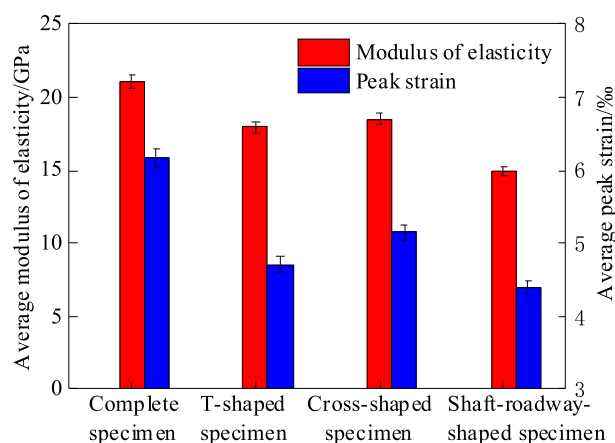


FIGURE 7. Deformation property of different specimens.

greater than those of the intersection-structure specimen and that the unloading rebound of the A-3 specimen thus occurred at the postpeak stage.

C. SPECIMEN ENERGY EVOLUTION LAW

Rock energy continually changes during the process of deformation. Rock deformation and failure is a state instability phenomenon driven by energy. Its essence is the sudden change in energy dissipation under certain conditions. Studying rock mechanical behavior from the perspective of energy can well explain rock failure characteristics. Energy input, energy accumulation, energy dissipation, and energy release always occur during rock deformation and failure. Energy absorption occurs before the peak and energy release occurs after the peak. The thermodynamic law is as follows:

$$U = U_e + U_d + U_0 \tag{1}$$

where U , U_e and U_d are input energy density, elastic energy density, and dissipative energy density, respectively. U_0 is energy density released by heat radiation and heat exchange, which is neglected.

Three types of energy density are calculated by the following formula (the energy calculation results are shown

in Tab. 2.):

$$\begin{cases} U = \sum_{i=1}^n \frac{1}{2} (\sigma_i + \sigma_{i+1}) (\varepsilon_i + \varepsilon_{i+1}) \\ U_e = \frac{\sigma_c^2}{2E_u} \\ U_d = U - U_e \end{cases} \tag{2}$$

where σ_i and ε_i are the stress and strain values at point i of the stress-strain curve, σ_c is the peak strength, and E_u is the unloading modulus on the unloading curve at the peak, which is approximate to that of elastic modulus.

The energy calculation results are shown in Tab. 2. The average energy absorption densities of the specimens are 261.38 kJ/m³, 155.74 kJ/m³, 164.68 kJ/m³, and 107.71 kJ/m³, their average energy dissipation densities are 41.64 kJ/m³, 49.62 kJ/m³, 52.96 kJ/m³, and 37.09 kJ/m³, and their energy dissipation ratios are 14.29%, 31.86%, 32.16%, and 34.43% respectively. The results show that the required energy for crack initiation, propagation and penetration is relatively small in the plastic deformation stage for complete specimens, but the energy is mainly accumulated in the elastic strain energy and the energy release after the peak is more intense and the ejection phenomenon occurs. The cracking energy of intersection structure specimens accounts for more than 30% of the absorbed energy, and their accumulated elastic strain energy is less than that of the complete specimens. At the same time, to quantitatively characterize the brittleness behavior of rock, the ratio of energy density after the peak to energy density before the peak is defined as the brittleness coefficient. The smaller the brittleness coefficient, the faster the elastic strain energy releases, the faster the stress falls, and the more significant is the brittleness behavior. The average brittleness coefficients of the four types of specimens (complete, T-shaped intersection structure, cross-shaped intersection structure, and shaft-roadway-shaped intersection structure) are 0.18, 0.26, 0.21 and 0.20, respectively. The order of brittleness degree of the four types of rocks is: complete specimen > shaft-roadway-shaped intersection structure specimen > cross-shaped intersection structure specimen > T-shaped intersection structure specimen.

V. FRACTURE EVOLUTION MECHANISM OF DIFFERENT SPECIMEN TYPES

A. STRESS DISTRIBUTION REGULARITIES IN SPECIMENS

Mastering the stress distribution around the prefabricated intersection-structure is necessary to reveal their deformation and failure mechanism. Because numerical simulations are fast and convenient, they were used to analyze the stress distribution around the intersection structure under the various kinds of specimens. First, four kinds of specimens were modeled by Midas/GTS with the powerful pretreatment function and then imported into FLAC3D for postprocessing analysis. Considering that crack initiation and propagation occur after the elastic stage, the constitutive model adopted the linear elastic model, and the above physical and mechanical parameters were taken as material parameters. Second, taking the center of the bottom surface of the specimen as the coordinate origin, the free boundary is the front, back, left and right sides of the specimen, the upper and lower end surfaces are fixed in the direction of x and y , and the loading is carried out by means of displacement control. Because the loading rate is measured in steps in numerical simulation, the average axial loading rate was set to 1.5×10^{-5} mm/step, and the specimen height was 0.15 m, which means that a microstrain was produced in each step. The definition of 2500 steps, i.e., the axial strain reaches 2.5 ‰, is equivalent to the stage of elastic deformation in the laboratory test, after which the loading rate of the upper and lower ends was set to 0 and automatically solved until the internal force was balanced. The stress distributions of four types of specimens were simulated as shown in Fig. 8.

From the principal stress distribution contour of Fig. 8, it can be seen that under uniaxial compression, the upper and lower ends were subject to x and y direction constraints that prevented the rock of the upper and lower ends from moving in x and y direction and resulted in stress concentration. Overall, the internal stress distribution of the specimen is well-distributed. The minimum principal stress of the complete specimen is 70 MPa, whereas that of the intersection structure specimen is approximately 100 MPa. The main reason is that the material parameters of the simulated void structure specimen are the same as that of the complete specimen. In the maximum principal stress contour (the tensile stress is positive and the compressive stress is negative), the internal stress of the complete specimen is compressive stress, which indicates that the failure mode is mainly the mixed failure of tension and shear dominated by compressive stress. A large tensile stress concentration is produced on the top and bottom plates of the intersection center of the specimens. Among them, the tensile stress of the tunnel specimen is the largest, 100 MPa, and that of the T-shaped intersection structure specimen and the cross-shaped intersection structure specimen are 80 MPa and 70 MPa, respectively, which all exceed the tensile strength of the rock. This shows that tensile failure first occurs at the top and bottom of the intersection point of the specimen and that the tensile crack growth rate of the cross-shaped intersection structure specimen is

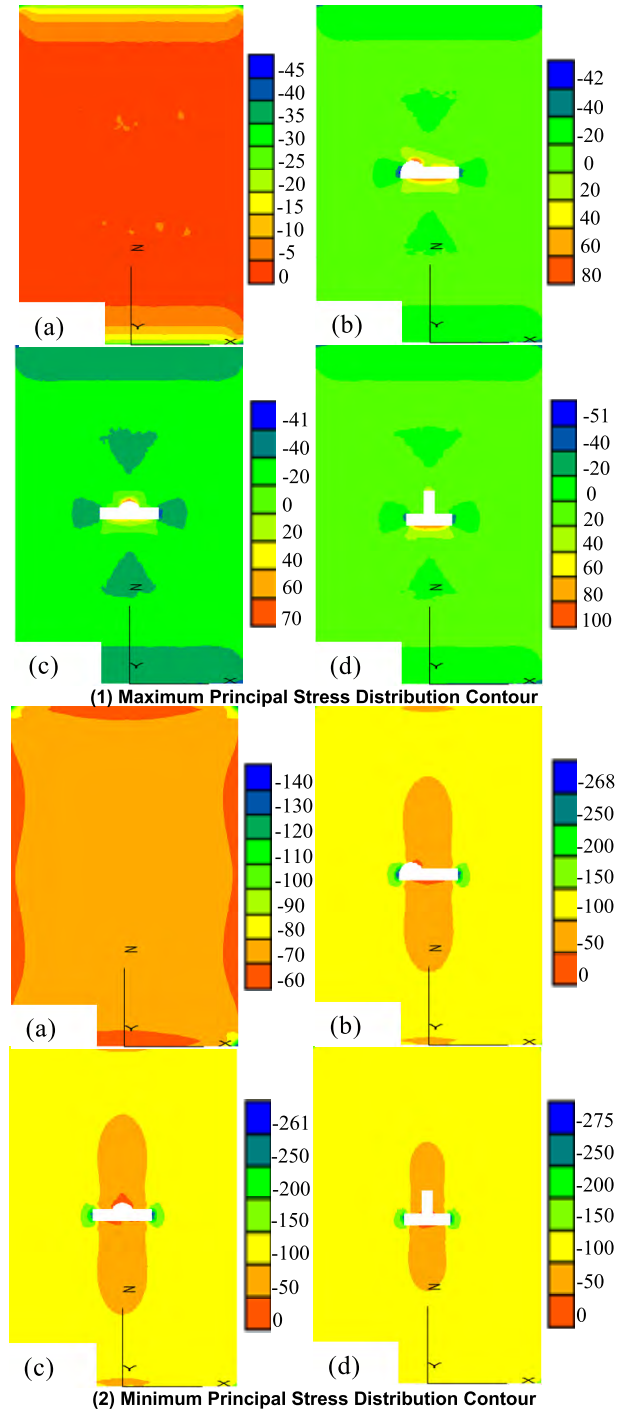


FIGURE 8. Principal stress distribution contours of specimens. (a) Complete specimen. (b) T-shaped intersection structure specimen. (c) Cross-shaped intersection structure specimen. (d) Shaft-roadway-shaped intersection structure specimen.

relatively slow. In addition, there are four fan-shaped and triangular compressive stress zones in the far field around the intersection structure, which are mainly caused by stress concentration and unloading; their locations are often at the boundary of stress concentration or unloading. In the minimal principal stress distribution contour of Fig. 8, all the stresses in the specimens are compressive, but there are long and

narrow unloading zones parallel to the loading direction at the top and bottom of the intersection, as well as different areas of fan-shaped stress concentration zones at the left and right sides. The stress concentration coefficient is $\sim 2-3$. The spalling ejection phenomena with plate cracking characteristics at the left and right sides of the intersection structure specimens, were observed in the laboratory tests, which is the macroscopic reflection of the compressive stress concentration. The order of compressive stress concentration is basically consistent with that of tensile stress concentration, i.e., shaft-roadway-shaped intersection structure specimen > T-shaped intersection structure specimen > cross-shaped intersection structure specimen. The main reason is that the more complex the intersection structure, the greater the stress concentration, and the stress concentration more easily occurs at the boundary of the straight-line hole than the circular-arc hole.

B. SURFACE CRACK PROPAGATION SPECIMEN REGULARITIES

The essence of the rock deformation and failure process is the process of crack initiation, propagation, and intersection leading to macroscopic failure. Therefore, mastering the regularities of crack initiation and evolution is an important prerequisite to reveal the progressive failure mechanism of rock. In this paper, DIC technology is used to capture speckle images of deformation at a different time in the loading process. The speckle images are calculated and analyzed by the GOM Correlate software. The entire surface strain field of specimens is obtained, and the fracture damage process of rock is reproduced. Due to the limitation of computer hardware configuration and transmission speed, it is unavoidable that the image captured by CCD in real time will lose its frame. The actual image acquisition speed is approximately 12 sheets/s. The results show that the principal strain can directly reflect the evolution process of crack initiation and propagation and can be used as an evaluation parameter to characterize the degree of rock deformation and failure. The principal strain field of four types of specimens under different stresses during loading are shown in Fig. 9. In the figure, σ and σ_c represent the axial stress and peak strength of a specimen, respectively, with units of MPa. The legend shows the magnitude of the strain in % units. In order to clearly describe the crack growth process, 'n^m' is used to represent different cracks and 'n' represents the crack type. Among them, '1' represents the tension crack, '2' represents the shear crack, '3' represents the far-field crack. In addition, 'm' represents the order in which cracks of the same type occur and is expressed in terms of a, b, c, etc.

At the initial stage of loading ($\sigma = 20$ MPa), high strain occurs at sporadic sites on the monitoring surface with an average tensile strain of 0.033%. The main reason is that the stress concentration at the tip of microcracks in rock during the stage of fracture compaction causes tension failure. Because of the random distribution of the high strain points and the small density in the region, the condition of

macrocracks cannot be reached. With the increase of stress ($\sigma = 50$ MPa), the high strain points near the main diagonal line of the specimen are densely distributed, but no cracks occur. The average strain value is approximately 0.100%. When the axial stress reaches approximately 90% of the peak stress, the principal strain significantly increases to 0.207%. Some microcracks on the main diagonal line of the specimen nucleate, and tension cracks 1^a parallel to the loading direction appear at the lower end of the right side of the specimen. When the axial stress approaches the peak strength, the tensile crack 1^b appears at the upper right end of the specimen, with an average strain of 0.221%. When the axial stress reaches the peak strength, a high strain point appears on the diagonal line of 1^a and 1^b cracks. The shear crack 2 begins to initiate, and the global strain is 0.192%. In the postpeak stage, the axial stress reaches 80 MPa and the average strain is 0.203%. Ejection failure occurs when tension cracks 1^a and 1^b penetrate to the edge of the plate, which penetrates to shear crack 2 and forms the V-shaped groove, which shows the typical characteristics of plate crack failure.

When the axial stress on the T-shaped intersection structure specimen is 20 MPa, tension cracks 1^a and 1^b parallel to the loading direction appear in the tension stress area of the top and bottom plate of the intersection point. The initiation crack stress is approximately 30% of the peak strength, and the average strain is 0.068%. When the axial stress increases to 51 MPa, the secondary tension crack 1^c parallel to the loading direction appears in the lower left corner of the arch tunnel. Meanwhile, the crack 1^a gradually closes and the average strain increases to 0.098%. When the axial stress increases to 52 MPa, shear crack 2 occurs in the upper corner of the right side of the hole and the wall of the hole spalls. When the axial stress continues to increase to 53 MPa, the secondary tension cracks 1^d parallel to the loading direction occur in the upper corner of the right side of the hole and the crack 1^b slowly closes, with an average strain of 0.114%. When the peak strength is reached, the initial tensile cracks 1^a and 1^b appear to be closed, and the average strain slightly increases to 0.122%. When the axial stress is 64 MPa after the peak, the average strain of the specimen decreases to 0.091% by crack closure, and the far-field crack 3 appears in the lower left corner of the subdiagonal line of the specimen. It is obvious that the initial tensile crack 1^a and 1^b are not necessarily the main ones that cause the macrodamage of the specimen.

The crack propagation mechanism of the cross-shaped intersection structure specimen is similar to that of the T-shaped intersection structure specimen. When the axial stress is 19 MPa, the vertical initial tension cracks 1^a and 1^b appear in the tensile stress concentration area at the top and the bottom plate of the intersection point, and it gradually expands with the increase of the stress until the axial stress is 59 MPa and the crack stops growing and begins to gradually close. Shear crack 2 on both sides of the hole appears because of spalling failure, and the strain increases from 0.044% to 0.097%. When the axial stress reaches 63 MPa, the vertical

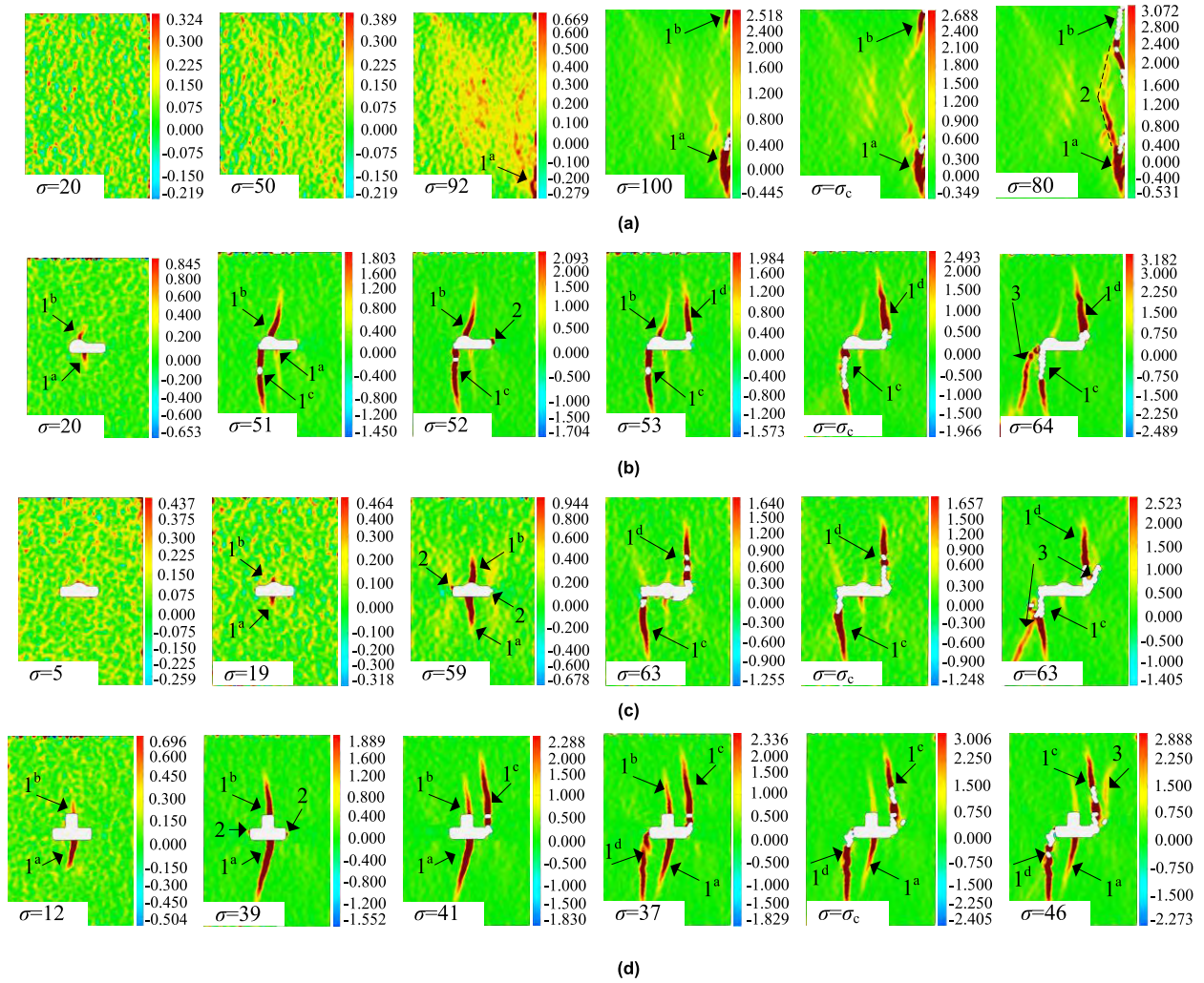


FIGURE 9. Fracture evolution of different specimens during axial loading. (a) Complete specimen (A-3). (b) T-shaped intersection structure specimen (B-3). (c) Cross-shaped intersection structure specimen (C-2). (d) Shaft-roadway-shaped intersection structure specimen (D-3).

secondary tensile cracks 1^c and 1^d occur at both the upper corner of the right side and the lower corner of the left side of the hole. At the same time, the initial tensile cracks 1^a and 1^b appear to close until the peak strength is reached, and the average strain increases from 0.117% to 0.129%. When the stress decreases to 63 MPa after the peak, the far-field crack 3 appears at the low corner of the subdiagonal line, and then penetrates with the secondary tension cracks 1^c and 1^d and causes specimen macrodamage.

The fracture evolution process of the cross-shaped intersection structure specimen is similar to that of the above two types of intersection specimen, i.e., tensile cracks 1^a and 1^b occur in the tensile stress concentration area around the cross-section under 30% peak stress, and gradually expand with the increase of stress until the axial stress is 39 MPa; then shear cracks 2 appear at the edges of both sides of the cross-section and spalling failure occurs. Then, the cracks 1^a and 1^b gradually close, and when the stress increases to 41 MPa, the secondary tension crack 1^c appears in the

upper corner of the right side of the cross structure. As the loading proceeds, the stress falls. When the stress is 37 MPa, the secondary tension cracks 1^d , 1^c and 1^d propagate with the increase of stress and 1^a and 1^b gradually close. When the postpeak stress is 46 MPa, a far-field crack 3 appears near the diagonal line at the upper right corner of the specimen and then penetrates with the secondary tension cracks 1^c and 1^d . The principal strain gradually increases from 0.060% of the crack initiation to 0.069% of the shear crack and 0.071% of the secondary tensile crack. The principal strain decreases after the peak and is 0.076% of the far-field crack.

It can be seen from the above that the macroscopic failure of the specimens occurs not at the peak but at the postpeak stage, regardless of the complete specimen or the intersection structure specimen. From the fracture evolution process of intersection structure specimens, it can be seen that the deformation and failure of specimens go through the initiation stage of initial tensile cracks, then the initial stage of tensile crack propagation and shear crack initiation, the nucleation

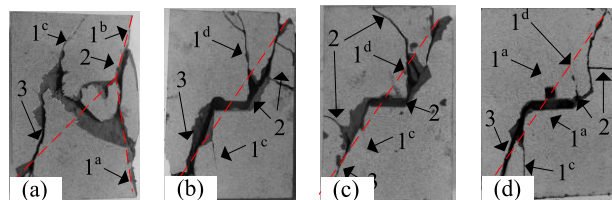


FIGURE 10. Failure modes of different types of rock specimens.
(a) Complete specimen. (b) T-shaped intersection structure specimen.
(c) Cross-shaped intersection structure specimen.
(d) Shaft-roadway-shaped intersection structure specimen.

and spalling stage of shear cracks, the rapid propagation stage of secondary tensile cracks, and the evolution and failure stage of postpeak far-field cracks. The initial tensile crack and secondary tensile crack propagate parallel to the loading direction. The initial tensile crack initiation stress is 30% of the peak strength. The generation of a secondary tensile crack has a compaction-inhibition effect on the initial tensile crack, which leads to its closure. Shear cracks often cause spalling failure on both sides of the intersection-structure. Far-field cracks initiate and propagate along the diagonal direction and penetrate with secondary tensile cracks, which results in the final failure of the specimens. In addition, the principal strain monitored during the fracture evolution stage increases with the increase of the axial stress and gradually decreases after the peak.

In summary, complete specimens are not easy to crack and have good stability. The existence of void defects in intersection-structure specimens weakens the physical and mechanical properties of rocks, and the stress concentration at the tip of the defects very easily cause rock instability and failure. In the intersection structure specimens, the arch boundary of the T-shaped intersection structure specimen is beneficial to restrain the spalling failure, and the propagation speed and length of tensile cracks are smaller in the tensile stress zone of the top and bottom of the intersection-point, which is better than that of the cross-shaped intersection structure specimen and the shaft-roadway-shaped intersection structure specimen. Cross-shaped intersection structure specimens have large tensile cracks at the top and bottom of the intersection point under the axial stress, and the existence of the shaft provides compensation space for the propagation of secondary tensile cracks, which promotes the initiation and propagation of secondary tensile cracks. The existence of secondary tensile cracks does not significantly inhibit the initial tensile cracks, which results in the worst measured stability of the specimens tested.

C. FAILURE MODE ANALYSIS OF SPECIMENS

The final failure modes of all kinds of specimens are shown in Fig. 10; the red lines in the figure are the main cracks of the specimens. It can be seen that Y-shaped tensile-shear failure occurs in the complete plate specimens under the progressive loading and that the shear failure dominated by the far-field crack generally occurs in intersection-structure specimens. Combined with the abovementioned fracture evolution

process, in the stage of far-field crack evolution and failure, the penetration of far-field crack and secondary tension crack is the main cause of macrofailures of the specimen. After penetration, some secondary tension cracks and shear cracks will still be induced, mainly because brittle hard rock accumulates high elastic strain energy during the loading process and the energy is released instantaneously when the load is sharply unloaded at the postpeak stage.

VI. CONCLUSIONS

1) The intersection structure has a significant weakening effect on the mechanical properties of rocks. The strength, modulus of elasticity and peak strain of different types of specimens have basically consistent evolution regularity, that is, complete specimens > cross-shaped intersection structure specimens > T-shaped intersection structure specimens > shaft-roadway-shaped intersection structure specimens.

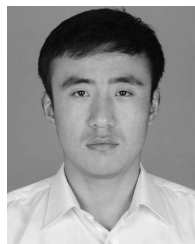
2) The energy required for crack initiation, propagation, and penetration of intersection structure specimens is approximately 30% in the plastic deformation stage. The energy required for cracking of intersection structure specimens is more than 30% of the energy absorbed and that of complete specimens is 14.29%. The order of brittleness degree of four types of specimens is: complete sample > shaft-roadway-shaped intersection structure specimens > cross-shaped intersection structure specimens > T-shaped intersection structure specimens.

3) The intersection structures are unloaded, which leads to tension stress concentration zones on the top and bottom slabs and fan-shaped compression stress concentration zones on both sides, with stress concentration coefficients of $\sim 2-3$. The more complex the intersection structure, the greater the stress concentration, and the stress concentration is more likely to occur at the boundary of the straight hole than at the boundary of the circular arc. The concentration degree of shaft-roadway-shaped intersection structure specimens is the largest and that of the sample of cross-shaped intersection structure specimens is the smallest.

4) The deformation and failure of intersection structure specimens go through a progression: the initiation stage of initial tensile cracks, the initial stage of tensile crack propagation and shear crack initiation, the nucleation and spalling stage of shear cracks, the rapid propagation stage of secondary tensile cracks, and the evolution and failure stage of postpeak far-field cracks. The initial tensile crack and secondary tensile crack propagate parallel to the loading direction. The initial tensile crack initiation stress is 30% of the peak strength. The generation of secondary tensile crack has a compaction inhibition effect on the initial tensile crack, which leads to its closure. Shear cracks often cause a spalling failure on both sides of the intersection structure. Far-field cracks initiate and propagate along the diagonal direction and penetrate with secondary tensile cracks, which results in the final failure of the specimens. Compared with Y-shaped tensile-shear failure of complete specimens, the mode of intersection structure specimens is shear failure.

REFERENCES

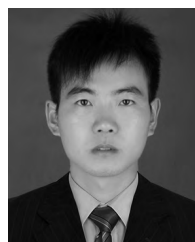
- [1] K. Hana, D. Conover, and K. Haramy, *Coal Mine Entry Intersection Behavior Study*. Pittsburgh, PA, USA: United States Bureau Mines, 1991, pp. 2–3.
- [2] S. Okubo and S. S. Peng, *Roof Bolting Patterns at Three-Way Entry Intersections*. Charlottesville, VA, USA: West Virginia Univ., 1978, pp. 23–24.
- [3] H. Gercek, *Stability of Intersections in Room-and-Pillar Coal Mining*. Philadelphia, PA, USA: Pennsylvania State Univ., 1982, pp. 148–149.
- [4] H. Gercek, “Stability considerations for underground excavation intersections,” *Mining Sci. Technol.*, vol. 4, no. 1, pp. 49–57, Oct. 1986.
- [5] J. Hematian, “Stability of roadways and intersections,” Ph.D. dissertation, Dept. Civil Mining Eng., Wollongong Univ., Wollongong, NSW, Australia, 1994.
- [6] R. N. Singh and I. P. J. Hematian, “Finite element analysis of three-way roadway junctions in longwall mining,” *Int. J. Coal Geol.*, vol. 45, nos. 2–3, pp. 115–125, Jan. 2001.
- [7] G. S. Esterhuizen, I. B. Tulu, and T. Klemetti, “Analysis of factors influencing coal mine intersection stability,” in *Proc. 48th US Rock Mech./Geomechanics Symp., Minneapolis: Amer. Rock Mech. Assoc.*, Jun. 2014, pp. 1–10.
- [8] B. Abbasi, *A numerical Analysis of Mine Intersections and Support Systems for Stability*. Carbondale, IL, USA: Southern Illinois Univ., 2010, pp. 152–153.
- [9] T. K. LU, B. H. Guo, and L. C. Cheng, “Numerical modeling for further understanding of roadway junction stability behaviour at deep underground,” *Int. J. Coal Sci. Technol.*, vol. 14, no. 1, pp. 38–43, Mar. 2008.
- [10] H. B. Chai, Y. B. Zhang, L. C. Cheng, and Y. F. Zou, “Research on deformation and stability of wall rocks in intersection of laneway in deep mine,” *J. Mining Saf. Eng.*, vol. 27, no. 2, pp. 200–204, 2010.
- [11] Z. Guo, J. Shi, J. Wang, F. Cai, and F. Wang, “Double-directional control bolt support technology and engineering application at large span Y-type intersections in deep coal mines,” *Int. J. Mining Sci. Technol.*, vol. 20, no. 2, pp. 254–259, Mar. 2010.
- [12] C. Ri-hong, C. Ping, Z. Ke, and L. Hang, “Stability analysis of roadway intersection considering strain softening,” *Rock Soil Mech.*, vol. 34, no. 6, pp. 1760–1821, Jun. 2013.
- [13] W.-S. Zhao, L.-J. Han, Z.-N. Zhao, and Q.-B. Meng, “Influence of principal stress on surrounding rock stability of roadway intersection,” *Rock and Soil Mech.*, vol. 36, no. 6, pp. 1752–1760, Jun. 2015.
- [14] N. B. Huang and D. H. Kong, “Study of reinforcement control technology and roof deformation of oblique cross with large section,” *J. Mining Saf. Eng.*, vol. 23, no. 2, pp. 249–252, 2006.
- [15] C. Wang, N. Zhang, G. C. Li, and J. Y. Chen, “Numerical simulation and support of roadway intersection,” *J. Mining Saf. Eng.*, vol. 25, no. 4, pp. 384–388, 2008.
- [16] X. Y. Wang, M. C. He, and S. B. Yang, “Failure mode of deep large section intersecting laneway and its countermeasures,” *J. Mining Saf. Eng.*, vol. 24, no. 3, pp. 283–287, 2007.
- [17] M. C. He, G. F. Li, A. W. Ren, and J. Yang, “Analysis of the stability of intersecting chambers in deep soft-rock roadway construction,” *J. China Univ. Mining Technol.*, vol. 37, no. 2, pp. 167–170, 2008.
- [18] Z.-B. Guo, P.-y. Guo, M.-H. Huang, and Y.-G. Liu., “Stability control of gate groups in deep wells,” *Mining Sci. Technol. (China)*, vol. 19, no. 2, pp. 155–160, Mar. 2000.
- [19] L. Xiang, *Deep Shaft Connecting Chambers Dynamic Response Model Experiment Research*. Huainan, China: Anhui Univ. Science Technology, 2009.
- [20] C. Hua et al., “Rock stability analysis and support countermeasure of chamber group connected with deep shaft,” *J. China Coal Soc.*, vol. 36, no. 2, pp. 261–266, Mar. 2011.
- [21] W. H. Peters and W. F. Ranson, “Digital imaging techniques in experimental stress analysis,” *Proc. SPIE*, vol. 21, no. 3, Jun. 1982, Art. no. 213427.
- [22] I. Yamaguchi, “A laser-speckle strain gauge,” *J. Phys. E, Sci. Instrum.*, vol. 14, no. 11, pp. 1270–1273, Nov. 1981.
- [23] B. Pan, K. Qian, H. Xie, and A. Asundi, “Two-dimensional digital image correlation for in-plane displacement and strain measurement: A review,” *Meas. Sci. Technol.*, vol. 20, no. 6, Apr. 2009, Art. no. 062001.



SHAOWEI MA received the B.S. degree in mineral resources engineering from the University of South China, Hengyang, China, in 2011, and the M.S. degree in mining engineering from Central South University, Changsha, China, in 2014, where he is currently pursuing the Ph.D. degree with the School of Resources and Safety Engineering. His current research interests include intelligent mining and rock mechanics.



ZHOUQUAN LUO received the Ph.D. degree in mining engineering from Central South University, Changsha, China, in 1999, where he is currently a Professor with the School of Resources and Safety Engineering. From 2003 to 2004, he was a Visiting Scholar with McGill University, Canada. His current research interests include dynamic monitoring of mine engineering disasters, and mine informatization and digitization. He has authored over 170 papers published in academic journals. He is the Director of the Seventh Council of China Nonferrous Metals Society, the Vice Chairman of the Mine Information Intelligence Committee of China Nonferrous Metals Society, and the Director of the Rock Mechanics and Engineering Degree of Hunan Province.



HAO WU received the B.S. degree in mining engineering from the Anhui University of Science and Technology, Anhui, China, in 2011, and the M.S. degree in mining engineering from Central South University, Hunan, China, where he is currently pursuing the Ph.D. degree in mining engineering with the School of Resources and Safety Engineering. He is also pursuing the Ph.D. Joint Training Program with The University of Arizona. His current research interests include rock mechanics and ground control in deep mining.



YAGUANG QIN received the B.S. degree in safety engineering from Henan Polytechnic University, Henan, China, in 2013, and the M.S. degree in safety engineering from Central South University, Hunan, China, in 2016, where he is currently pursuing the Ph.D. degree in safety science and engineering.

His research interests include mine safety mining technology and the multi-field coupling of rock mass.

Mr. Qin's awards and honors include the National Scholarship for Graduate Students, and the Outstanding Graduate Students and the Outstanding Graduates from Central South University.

• • •